# Effects of thermal diffuse scattering and surface tilt on diffraction and channeling of fast electrons in CdTe

L. J. Allen
*School of Science and Mathematics Education, University of Melbourne, Parkville, Victoria 3052, Australia*

C. J. Rossouw
*Division of Materials Science and Technology, Commonwealth Scientific and Industrial Research Organisation (CSIRO), Locked Bag 33, Clayton, Victoria 3168, Australia*

(Received 22 August 1988; revised manuscript received 21 December 1988)

A Bloch-wave model for propagating a fast-electron wave through a noncentrosymmetric crystal for non-normal incidence is discussed, as well as approximations for linearizing the equations. Calculations which simulate {111} systematic row diffraction conditions in CdTe are used to illustrate how the tilt of the surface with respect to the diffracting planes affects the fast-electron wave function in the crystal. The influence of thermal diffuse scattering (TDS) removes possible ambiguity from the interpretation of "ALCHEMI-type" experiments [J. C. H. Spence and J. Taftø, J. Microsc. **130**, 147 (1983)] in determining the polarity of noncentrosymmetric crystals. The inclusion of mean and anomalous absorption, using a quantitative Einstein model for TDS, allows direct correlation between theory and experiment for convergent-beam electron diffraction, again allowing direct measurement of crystal polarity.

## I. INTRODUCTION

Electron-beam methods for determining the structure-factor phase or polarity of noncentrosymmetric crystals rely on accurate measurement of diffracted intensities by using selected-area diffraction,[1] or, more conveniently, from convergent-beam diffraction patterns.[2,3] Alternatively, variation of characteristic x-ray emission ratios[4] with orientation may be used to determine the polarity, as reported by Taftø[5] for GaAs and InP. Electron-diffraction procedures require correlation between theory and experiment of diffracted beam intensities as a function of thickness and orientation. Variations in characteristic x-ray yield is related to a thickness-averaged ($z$-dependent) value of fast-electron probability density $\psi\psi^*$ on the different atomic species.[6,7]

Diffraction theory related to non-normal-incidence electrons impinging onto a crystal has shown how diffracted beam intensities are susceptible to crystal tilt.[8–10] It is also necessary to consider comparatively large surface tilts in the theory of an $(e,2e)$ reaction in a crystal, in which incident-, scattered-, and ejected-electron wave functions are described dynamically.[11] However, no work on the effects of surface tilt on the $z$ dependence of $\psi\psi^*$ on specific sites in the unit cell has been reported to date. In modern analytical microscopes it is often necessary to tilt at least 20° towards a low-angle x-ray detector for energy-dispersive x-ray analysis (EDX) spectral acquisition. With a limited angular range available for setting up desired dynamical conditions for ALCHEMI experiments, it is thus often necessary to use tilts of 45°, and up to 60° in more extreme cases.

We present a concise theory on the influence of surface tilt. Electron scattering in CdTe under systematic (111) row (noncentrosymmetric) diffraction conditions is simulated to predict effects of surface tilt on $\psi\psi^*$ and diffracted beam intensities.

We use a detailed model to include dechanneling effects due to thermal diffuse scattering (TDS), and to determine the response of diffracted beams in noncentrosymmetric crystals. An Einstein model for TDS is used to determine the absorptive (imaginary) potential, and first-order perturbation theory yields the anomalous absorption coefficients. Consideration of dechanneling and diffraction contrast, including the full anomalous absorption corrections, enables direct determination of polarity of noncentrosymmetric crystals. This work is related to electron-scattering experiments on cross sections of $Hg_xCd_{1-x}Te$ layers grown by organometallic chemical vapor deposition (MOCVD) onto GaAs substrates under various conditions.[12,13]

## II. THE SURFACE IN DYNAMICAL THEORY

A starting point for formulating a general theory of electron diffraction in a crystal is the well-known dynamical equations of Bethe:[14]

$$[K^2-(\mathbf{k}^i+\mathbf{g})^2]C_g^i+\sum_{h\,(\neq g)}U_{g-h}C_h^i=0\ , \tag{1}$$

there being one such equation for each Bloch wave on branch $i$ of the dispersion surface. $K^2=\chi^2+U_0$, where $\chi$ is the wave vector of the incident electron in vacuum and $U_0$ related to the mean inner crystal potential. By allowing the Fourier coefficients $f(\mathbf{g}-\mathbf{h})$ of the scattering potential of an isolated atom to become complex, we include mean and anomalous absorption phenomena. The absorptive (imaginary) potential may be included in the crystal $U$'s, i.e.,

$$U_{g-h}\rightarrow U_{g-h}+iU'_{g-h}\ , \tag{2}$$

by

$$U'_{g-h}=\sum f'_{\beta n}(\mathbf{g}-\mathbf{h})\exp[-i(\mathbf{g}-\mathbf{h})\cdot\tau_{\beta n}]\ , \tag{3}$$

 

where the summation is over all atomic species $\beta$ in the positions $\tau_{\beta n}$ within the unit cell. The boundary condition at the crystal surface, i.e., that all Bloch wave vectors $\mathbf{k}^i$ must have the same tangential component along the surface (see Fig. 1), allows us to express each $\mathbf{k}^i$ in the form

$$\mathbf{k}^i=\mathbf{K}+\lambda^i\hat{\mathbf{n}}=\mathbf{K}+(\gamma^i+i\eta^i)\hat{\mathbf{n}}\ , \tag{4}$$

where we explicitly decompose the complex eigenvalue $\lambda^i$ into its real part $\gamma^i$ (the *anpassung*) and imaginary part $\eta^i$ (the absorption coefficient). $\hat{\mathbf{n}}$ is a unit vector in the direction of the surface normal, directed into the crystal. Using Eq. (4), we may rewrite Eq. (1) in the form

$$[-(\lambda^i)^2-\lambda^i P_g+Q_g]C_g^i+\sum_{h\,(\neq g)}U_{g-h}C_h^i=0 \tag{5}$$

for each $i$, where

$$P_g=2\hat{\mathbf{n}}\cdot(\mathbf{K}+\mathbf{g}) \tag{6}$$

and

$$Q_g=-\mathbf{g}\cdot(2\mathbf{K}+\mathbf{g})+iU_0'\ . \tag{7}$$

In matrix notation, Eq. (5) can be written as

$$\begin{bmatrix} Q_0 & U_{-g} & U_{-h} & \cdots \\ U_g & Q_g & U_{g-h} & \cdots \\ U_h & U_{h-g} & Q_h & \cdots \\ \vdots & \vdots & \vdots & \ddots \end{bmatrix} -\lambda^i \begin{bmatrix} P_0 & 0 & 0 & \cdots \\ 0 & P_g & 0 & \cdots \\ 0 & 0 & P_h & \cdots \\ \vdots & \vdots & \vdots & \ddots \end{bmatrix} -(\lambda^i)^2 \begin{bmatrix} 1 & 0 & 0 & \cdots \\ 0 & 1 & 0 & \cdots \\ 0 & 0 & 1 & \cdots \\ \vdots & \vdots & \vdots & \ddots \end{bmatrix} \begin{bmatrix} C_0^i \\ C_g^i \\ C_h^i \\ \vdots \end{bmatrix} = \begin{bmatrix} 0 \\ 0 \\ 0 \\ \vdots \end{bmatrix} . \tag{8}$$

A method for solving this nonlinear system of equations for the $\lambda^i$'s and $C_g^i$'s without approximations has been given by Kim and Sheinin.[15] An approximation, which is excellent[15] for energetic electrons and values of the angle $\theta$ between the surface normal and diffracting planes (see Fig. 1) of up to 80°, is to linearize Eq. (8) by ignoring the $(\lambda^i)^2$ term. Equation (8) then reduces to a generalized eigenvalue problem

$$\begin{bmatrix} Q_0 & U_{-g} & U_{-h} & \cdots \\ U_g & Q_g & U_{g-h} & \cdots \\ U_h & U_{h-g} & Q_h & \cdots \\ \vdots & \vdots & \vdots & \ddots \end{bmatrix} \begin{bmatrix} C_0^i \\ C_g^i \\ C_h^i \\ \vdots \end{bmatrix} =\lambda^i \begin{bmatrix} P_0 & 0 & 0 & \cdots \\ 0 & P_g & 0 & \cdots \\ 0 & 0 & P_h & \cdots \\ \vdots & \vdots & \vdots & \ddots \end{bmatrix} \begin{bmatrix} C_0^i \\ C_g^i \\ C_h^i \\ \vdots \end{bmatrix} . \tag{9}$$

The eigenvalues and eigenvectors (which are only orthogonal if all the $P_g$'s are equal) can be obtained using standard methods. However, multiplying through from the left by the inverse of the diagonal matrix containing the $P_g$'s, we can recast Eq. (9) into the form

$$\begin{bmatrix} Q_0/P_0 & U_{-g}/P_0 & U_{-h}/P_0 & \cdots \\ U_g/P_g & Q_g/P_g & U_{g-h}/P_g & \cdots \\ U_h/P_h & U_{h-g}/P_h & Q_h/P_h & \cdots \\ \vdots & \vdots & \vdots & \ddots \end{bmatrix} \begin{bmatrix} C_0^i \\ C_g^i \\ C_h^i \\ \vdots \end{bmatrix} =\lambda^i \begin{bmatrix} C_0^i \\ C_g^i \\ C_h^i \\ \vdots \end{bmatrix} , \tag{10}$$

where the square matrix is only Hermitian for no absorption potential and provided that all the $P_g$'s are equal.[16] The approximation which ignores the $(\lambda^i)^2$ term is better than approximations usually made[17] (often for $\theta=0°$ and small $\alpha$) which retain elements of $(\lambda^i)^2$, as has been demonstrated by Kim and Sheinin.[15] Having solved the eigenvalue problem given by Eq. (8) to obtain the complex $\lambda^i$'s and $C_g^i$'s, it remains to obtain the excitation coefficients $A^i$ in the Bloch-wave expansion of the wave function, i.e.,

$$\psi(\mathbf{K},\mathbf{r})=\sum_i A^i\sum_g C_g^i\exp[i(\mathbf{K}+\lambda^i\hat{\mathbf{n}}+\mathbf{g})\cdot\mathbf{r}]\ . \tag{11}$$

This has been discussed by Sheinin and Jap.[18] If $\underline{C}^{-1}$ is the inverse of the matrix which has the eigenvectors as columns, then $A^i=C_i^{-1}$, where $C_i^{-1}$ is the $i$th element of the first column of $\underline{C}^{-1}$. It is convenient to normalize the eigenvectors by

$$\sum_g C_g^{i*}C_g^i=1\ . \tag{12}$$

## III. TDS AND ANOMALOUS ABSORPTION

Fourier coefficients $f'(\mathbf{g}-\mathbf{h})$ of the absorption potential may be derived from an Einstein model for TDS from isolated atoms, i.e.,[19–21]

$$f'_\beta(\mathbf{g}-\mathbf{h})=(n_\beta k/4\pi^2)\int_0^{2\pi}d\phi\int_0^{\pi}d\theta\sin\theta f_\beta(-\mathbf{q}-\mathbf{h})f_\beta(-\mathbf{q}-\mathbf{g})\{\exp[-M(\mathbf{g}-\mathbf{h})]-\exp[-M(-\mathbf{q}-\mathbf{g})-M(-\mathbf{q}-\mathbf{h})]\}, \tag{13}$$

where $n_\beta$ is the density of atoms of type $\beta$ in the crystal, and $f_\beta(\mathbf{q})$ the relativistic atomic scattering factor for a wave-vector transfer $\mathbf{q}=\mathbf{k}-\mathbf{k}'$. The Debye-Waller factor $M(q)=\frac{1}{2}q^2\langle u_\beta^2\rangle$, where $\langle u_\beta^2\rangle$ is the projected mean-square atomic displacement. The angle $\theta$ defines the angle between the incident and scattered wave vectors $\mathbf{k}$ and $\mathbf{k}'$, with $\phi$ being the azimuthal angle. The Fourier coefficients $U'_{g-h}$ of the absorption potential within the crystal are obtained from the single atom coefficients $f'(\mathbf{g}-\mathbf{h})$ via Eq. (3). The kinematical mean free path $\lambda_{\mathrm{TDS}}$ for a plane wave may be derived from Eq. (13), i.e.,[22,23]

$$\frac{d\lambda_{\mathrm{TDS}}^{-1}}{d\Omega}=\sum_\beta n_\beta f_\beta^2(q)[1-\exp(-\langle u_\beta^2\rangle q^2)] . \tag{14}$$

$\lambda_{\mathrm{TDS}}$ is obtained by numerical integration of Eq. (14) over $\Omega$. Direct insertion of the absorptive potential into the square matrix in Eq. (10) yields complex eigenvalues which account for mean and anomalous absorption on each branch $i$ of the dispersion surface. However, it is adequate and has computational advantages to treat absorption perturbatively. We generalize the perturbative approach outlined by Humphreys,[17] yielding the absorption coefficient $\eta^i=\mathrm{Im}(\lambda^i)$, which attenuates $A^i$ by $\exp(-\eta^i\hat{\mathbf{n}}\cdot\mathbf{z})$. Treating absorption as a first-order perturbation, we may write [cf. Eqs. (1)–(4)]

$$\{K^2-[\mathbf{K}+(\gamma^i+i\eta^i)\hat{\mathbf{n}}+\mathbf{g}]^2\}C_g^i+\sum_{h\,(\neq g)}U_{g-h}C_h^i+i\sum_h U'_{g-h}C_h^i=0 . \tag{15}$$

Subtracting Eq. (15) from the case where there is no absorption, one obtains

$$-(\eta^i)^2+2\eta^i(\hat{\mathbf{n}}\cdot\mathbf{K}+\hat{\mathbf{n}}\cdot\mathbf{g}+\eta^i\gamma^i)C_g^i=\sum_h U'_{g-h}C_h^i . \tag{16}$$

Since $\eta^i$ is small, we can approximate this as

$$\eta^i P_g C_g^i=\sum_h U'_{g-h}C_h^i , \tag{17}$$

where $P_g$ is given by Eq. (6). Multiplying through from the left by $C_g^{i*}$, and by summing over all $g$, we obtain

$$\eta^i=\sum_{g,h}C_g^{i*}U'_{g-h}C_h^i\Big/\left[\sum_g P_g C_g^{i*}C_g^i\right] . \tag{18}$$

The $\eta^i$ terms vary with orientation. We assume that TDS provides the dominant mechanism for anomalous absorption and "dechanneling" of the fast electron, and that the thermally scattered component provides a "kinematic" background component to the peaking of $\psi\psi^*$ on atomic sites. Low-energy plasmon excitations are forward peaked and do not contribute substantially to dechanneling, and high-angle electronic excitations have a relatively small cross section.

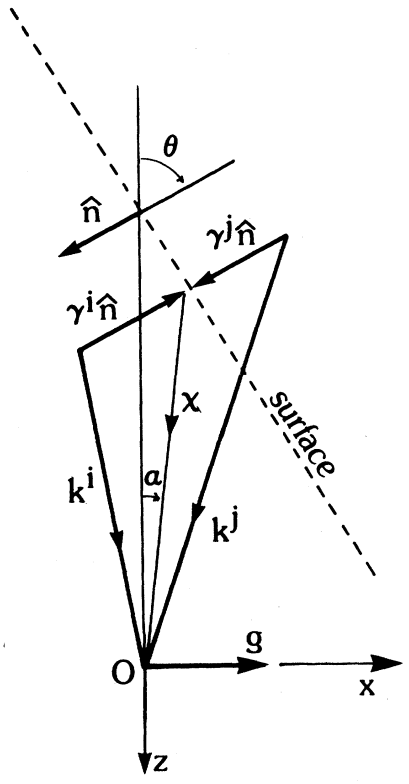


FIG. 1. Reciprocal-space diagram defining the angle $\theta$ which describes the tilt of the surface relative to the $z$ coordinate, with reciprocal lattice vector $\mathbf{g}$ perpendicular to $\mathbf{z}$. The incident wave vector $\chi$ is at an angle $\theta$ to $\mathbf{z}$ (or the diffracting planes), and the eigenvalue separation $\Delta\gamma$ occurs along the surface normal $\hat{\mathbf{n}}$. The wave vectors $\mathbf{k}^i$ and $\mathbf{k}^j$ have different $x$-$y$ components if $\theta\neq 0°$.

## IV. PROBABILITY DENSITY AS A FUNCTION OF DEPTH

Let $\mathbf{r}_0$ be the position vector of the origin of a unit cell on the surface of the crystal. Any point $\mathbf{r}$ in a unit cell below this along the $z$ direction, with origin at the point $\mathbf{r}_1$, can be written as (see Fig. 2) $\mathbf{r}=\mathbf{r}_1-\mathbf{r}_0+\boldsymbol{\tau}=\mathbf{z}+\boldsymbol{\tau}$, where $\boldsymbol{\tau}$ is a vector relative to the origin of the unit cell $\mathbf{r}_1$. The vector $\mathbf{z}=\mathbf{r}_1-\mathbf{r}_0$ gives a displacement from the surface of the origin of a unit cell within the crystal, measured along $\mathbf{z}$. From Eq. (11) it follows that

$$\psi(\mathbf{K},\mathbf{z}+\tau)\psi^*(\mathbf{K},\mathbf{z}+\tau)=\sum_{i,j} A^i A^{j*} \sum_{g,h} \exp[i(\mathbf{g}-\mathbf{h})\cdot\tau]\exp[-(\eta^i+\eta^j)\hat{\mathbf{n}}\cdot(\mathbf{z}+\tau)]C_g^i C_h^{j*}\exp\{i[(\gamma^i-\gamma^j)\hat{\mathbf{n}}\cdot(\mathbf{z}+\tau)]\} \ . \quad (19)$$

The probability density $\psi\psi^*$ on atoms of a particular type $\beta$ in the unit cell can be found by summing over the appropriate sites $\tau_\beta$. The absorption terms reduce the dynamic component to the fast-electron wave function with increasing $z$. The net intensity loss from the dynamical wave function at a depth $z$ may be obtained by finding the sum of diffracted beam intensities, where absorption due to TDS is accounted for. The intensity of each beam is given by

$$I_g=\left|\sum_i A^i \exp(-\eta^i\hat{\mathbf{n}}\cdot\mathbf{z})C_g^i\exp(i\gamma^i\hat{\mathbf{n}}\cdot\mathbf{z})\right|^2 , \quad (20)$$

and thus the thermally scattered component $I_{\mathrm{TDS}}$ at a depth $z$ is

$$I_{\mathrm{TDS}}=1-\sum_g I_g(z) \ . \quad (21)$$

Assuming that the TDS component provides a kinematical "plane-wave" component to $\psi\psi^*$ on the atomic sites, a $z$-averaged result for $\psi\psi^*$ on a particular site $\tau$ within the unit cell, integrated through the distance $d$ traversed in the crystal, may be written analytically as[7]

$$\psi\psi^*_{\mathrm{av}}=d^{-1}\int_0^d(\psi\psi^*+I_{\mathrm{TDS}})dz \quad (22)$$

and, using Eqs. (16)–(19), with the approximation that $(\eta^i+\eta^j)\hat{\mathbf{n}}\cdot\tau$ and $(\gamma^i-\gamma^j)\hat{\mathbf{n}}\cdot\tau$ are small, $\psi\psi^*_{\mathrm{av}}$ is

$$1+\sum_{i,j} A^i A^{j*}\frac{(\eta_z^i+\eta_z^j)+i(\gamma_z^i-\gamma_z^j)}{(\eta_z^i+\eta_z^j)^2+(\gamma_z^i-\gamma_z^j)^2}\frac{\{1-\exp[-(\eta_z^i+\eta_z^j)d]\exp[i(\gamma_z^i-\gamma_z^j)d]\}}{d}\sum_{g,h}\{C_g^i C_h^{j*}\exp[i(\mathbf{g}-\mathbf{h})\cdot\tau]-C_g^i C_g^{j*}\} \ , \quad (23)$$

where the subscript $z$ indicates the $z$ components of $\gamma$ and $\eta$. Equation (23) effectively accounts for dynamical peaking of the fast-electron wave function and dechanneling due to TDS.

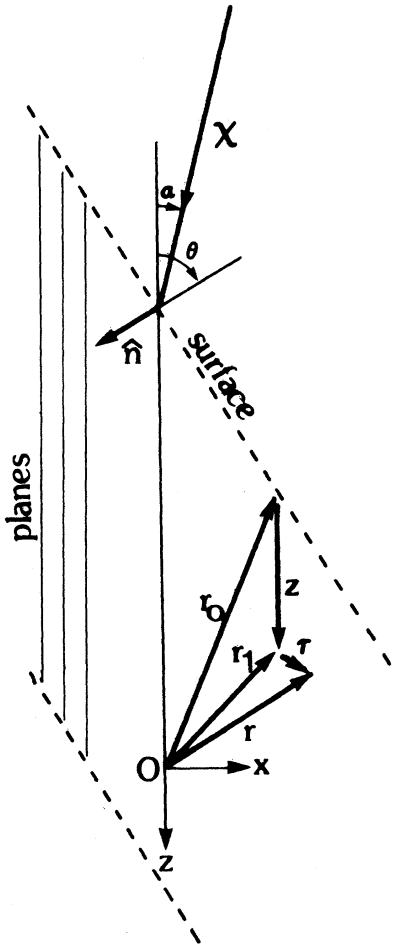


FIG. 2. Real-space diagram, defining coordinate system and angles $\theta$, $\alpha$, and the surface normal $\hat{\mathbf{n}}$ relative to the surface and a set of diffracting planes. The vectors $\mathbf{r}$, $\mathbf{r}_0$, and $\mathbf{r}_1$ are introduced in the text. $\tau$ is a displacement vector from the origin of a unit cell.

## V. CRYSTAL STRUCTURE AND SCATTERING

CdTe has the ZnS (zinc-blende) structure with lattice parameter $a_0=0.6482$ nm. A projection of the crystal structure viewed down a $\langle 110\rangle$ zone axis is shown in Fig. 3(a). Clearly, in each of the three $\{111\}$ planes shown over the [111] repeat distance, rows of Cd and Te atoms are separated by $\Delta x=\frac{1}{12}a_0[1,1,1]$, i.e., $\Delta x=0.09356$ nm. The $\{111\}$ polar surface has two types of faces,[24] $A$ or $B$. If the [111] direction is directed outwards from the surface, this is terminated by a triply bonded Cd atom or singly bonded Te atom. This is also known as the (111) $A$ face or Cd face since the stable configuration has Cd atoms on the surface. Conversely, if the [111] direction faces into the surface, this is the $(\bar{1}\bar{1}\bar{1})$ $B$ face, or Te face.

We use the Debye-Waller factors supplied by Reid[25] for CdTe to account for thermal attenuation of the Fourier coefficients $V_g$, where at 300 K $\langle u_\beta^2\rangle$ of Cd and Te are $2.47\times10^{-4}$ and $1.65\times10^{-4}$ nm$^2$, respectively. Complex scattering potentials for various pairs of beams in the $\{111\}$ systematic row are given in Table I, using the Mott formula to convert Doyle-Turner[26] or Cromer-Waber[27] scattering factors for x rays to electron scattering factors at 300 K. The unit cell origin is chosen midway between Cd-Te atomic pairs, and the set of Cd atoms occupying fcc positions $(-1/8,-1/8,-1/8)$, and the Te atoms occupying fcc positions $(+1/8,+1/8,+1/8)$ in the unit cell. The $U_0$ term is 12.89 eV.

Thus the imaginary component in the (111) structure factor is about 9% of the real part, and the phase angle inverts for the $(\bar{1}\bar{1}\bar{1})$ structure factor. The (222) and (666) components, zero for a diamond-type lattice, result from differences in the Cd and Te atomic scattering factors.

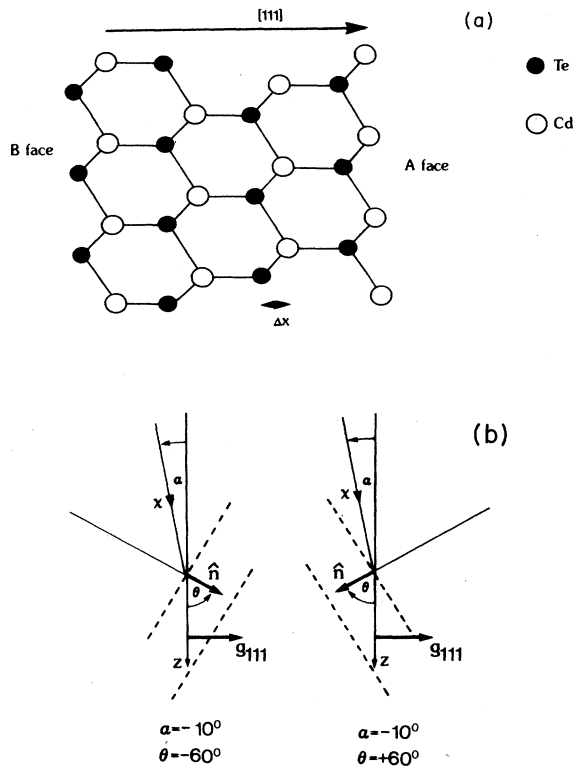


FIG. 3. (a) The CdTe structure viewed along $y=[1\bar{1}0]$. The $x$ direction corresponds to [111] and the $z$ direction to $[\bar{1}\,\bar{1}\,2]$. $\{111\}$ planes are polar, with projected displacements of the Cd and Te atoms of $\Delta x=0.0936$ nm. The (111) $A$ (Cd) surface and $(\bar{1}\,\bar{1}\,\bar{1})$ $B$ (Te) surface are indicated. (b) Geometry of crystal relative to the $z$ direction for $\theta=-60°$ and 60°.

## VI. COMPUTED RESULTS

Fifteen beam $\{111\}$ systematic row calculations were performed to determine the wave function $\psi(\mathbf{k},\mathbf{r})$ from the set of Bloch waves excited in the crystal. These are nonorthogonal sets[16] when the surface normal $\hat{\mathbf{n}}$ is not parallel to the incident electron wave vector $\chi$. Unless otherwise stated, an incident beam energy of 120 keV is simulated.

(i) $\lambda_{TDS}$. $\lambda_{\mathrm{TDS}}$ as a function of surface tilt and orientation is shown in Fig. 4, assuming a temperature of 300 K. These values are determined numerically by finding the value of $z$ where the summed intensity of all diffracted beams $I_g$ from Eq. (17) is equal to $\exp[-1]$. Note the reduction in $\lambda_{\mathrm{TDS}}$ near the exact $\{111\}$ orientation. For zero surface tilt, there is a slight asymmetry about the symmetrical Laue orientation. The asymmetry is enhanced for surface tilts of 60° and −80° as indicated. Thus the influence of dynamical scattering and surface tilt on $\lambda_{\mathrm{TDS}}$ leads to rapid changes as diffracted beams are brought through the Ewald sphere. The kinematic mean free path is 61 nm.

(ii) $\psi\psi^*$. Calculations of fast-electron probability density $\psi\psi^*$ on Cd or Te atomic sites as a function of distance traversed in the z direction are shown in Fig. 5 for the symmetrical Laue orientation. Here we have neglected TDS to highlight the effect of surface tilt on the dynamical wave function. For $\theta=0°$ in Fig. 5(a), $\psi\psi^*$ peaks preferentially on Te, oscillating with $z$ in phase with bright field extinction phenomena. For a surface tilt of 60° in Fig. 5(b), subtle changes in the fine structure of $\psi\psi^*(z)$ occur for both Cd and Te. For a tilt of −80° in Fig. 5(c), stronger effects are predicted. However, the overall nature and shape of $\psi\psi^*(z)$ remains similar.

The (111) Bragg orientation is simulated in Fig. 5(d) for $\theta=0°$. $\psi\psi^*$ initially peaks strongly on Te, peaking at about half an extinction distance, after which $\psi\psi^*$ peaks strongly on Cd. For the $(\bar{1}\,\bar{1}\,\bar{1})$ Bragg orientation in Fig. 5(e), the $z$ dependence of $\psi\psi^*$ on Cd and Te inverts, apart from some small differences. Fine detail in the $z$ dependence of $\psi\psi^*$ occurs for various surface tilts, similar to Figs. 5(b) and 5(c).

Dechanneling plus the TDS component at 300 K, from Eq. (23), is simulated in Fig. 6 for the symmetrical and $\pm g_{(111)}$ Bragg orientations. With increasing depth $\psi\psi^*_{\mathrm{av}}$ on each site approaches unity. $\psi\psi^*$(Te) as a function of orientation and surface tilt at 300 K is shown in Fig. 7(a). Note that $\psi\psi^*$ maximizes at the (111) Bragg orientation for $z=22$ nm. A similar plot for Cd is shown in Fig. 7(b),

TABLE I. Complex potentials for beams in a $\{111\}$ systematic row.

| Beam index $h\ k\ l$ | Scattering potentials in eV at 300 K: Real part | Imaginary part | Extinction distance at 120 keV $\xi_g$ (nm) |
|---|---|---|---|
| 1 1 1 | −6.80 | −0.62 | 53.3 |
| $\bar{1}\ \bar{1}\ \bar{1}$ | −6.80 | 0.62 | |
| 2 2 2 | 0.0 | 0.40 | 910.5 |
| $\bar{2}\ \bar{2}\ \bar{2}$ | 0.0 | −0.40 | |
| 3 3 3 | 2.26 | −0.18 | 160.5 |
| $\bar{3}\ \bar{3}\ \bar{3}$ | 2.26 | 0.18 | |
| 4 4 4 | −1.84 | 0.0 | 197.5 |
| $\bar{4}\ \bar{4}\ \bar{4}$ | −1.84 | 0.0 | |
| 5 5 5 | 0.74 | 0.13 | 483.2 |
| $\bar{5}\ \bar{5}\ \bar{5}$ | 0.74 | −0.13 | |
| 6 6 6 | 0.0 | −0.14 | 2543.9 |
| $\bar{6}\ \bar{6}\ \bar{6}$ | 0.0 | 0.14 | |

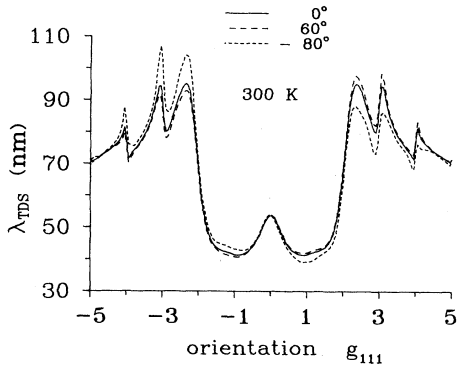


FIG. 4. Computed values of $\lambda_{TDS}$ at 120 keV for a {111} systematic row diffraction condition for CdTe. Note fluctuations as successive Brillouin-zone boundaries are crossed, as well as the influence of surface tilt $\theta$.

where $\psi\psi^*$ maximizes at the $(\bar{1}\,\bar{1}\,\bar{1})$ Bragg orientation.

For ALCHEMI-type experiments, the observed ratio Te/Cd of characteristic x-ray emission depends on the $z$-integrated ratio, $\psi\psi^*_{av}$. This is a function of $z$, orientation, and temperature. Figure 8(a) shows the computed ratio $\psi\psi^*_{av}$(Te/Cd) as a function of $z$ and orientation at 300 K. Note that the ratio is always larger for the (111) Bragg orientation than for the $(\bar{1}\,\bar{1}\,\bar{1})$ Bragg orientation and that the peaking of this ratio is quite broad in orientation space. If TDS is neglected, as in Fig. 8(b), this ratio may be enhanced for the $(\bar{1}\,\bar{1}\,\bar{1})$ Bragg orientation for a particular range of $z$. In addition, fine detail in this ratio occurs as the orientation changes from $(\bar{1}\,\bar{1}\,\bar{1})$ to (111) Bragg orientation. A 400-keV beam with the target at 300 K is simulated in Fig. 8(c). Thus TDS scattering ensures that the peaking of $\psi\psi^*$ within the first extinction period pro-

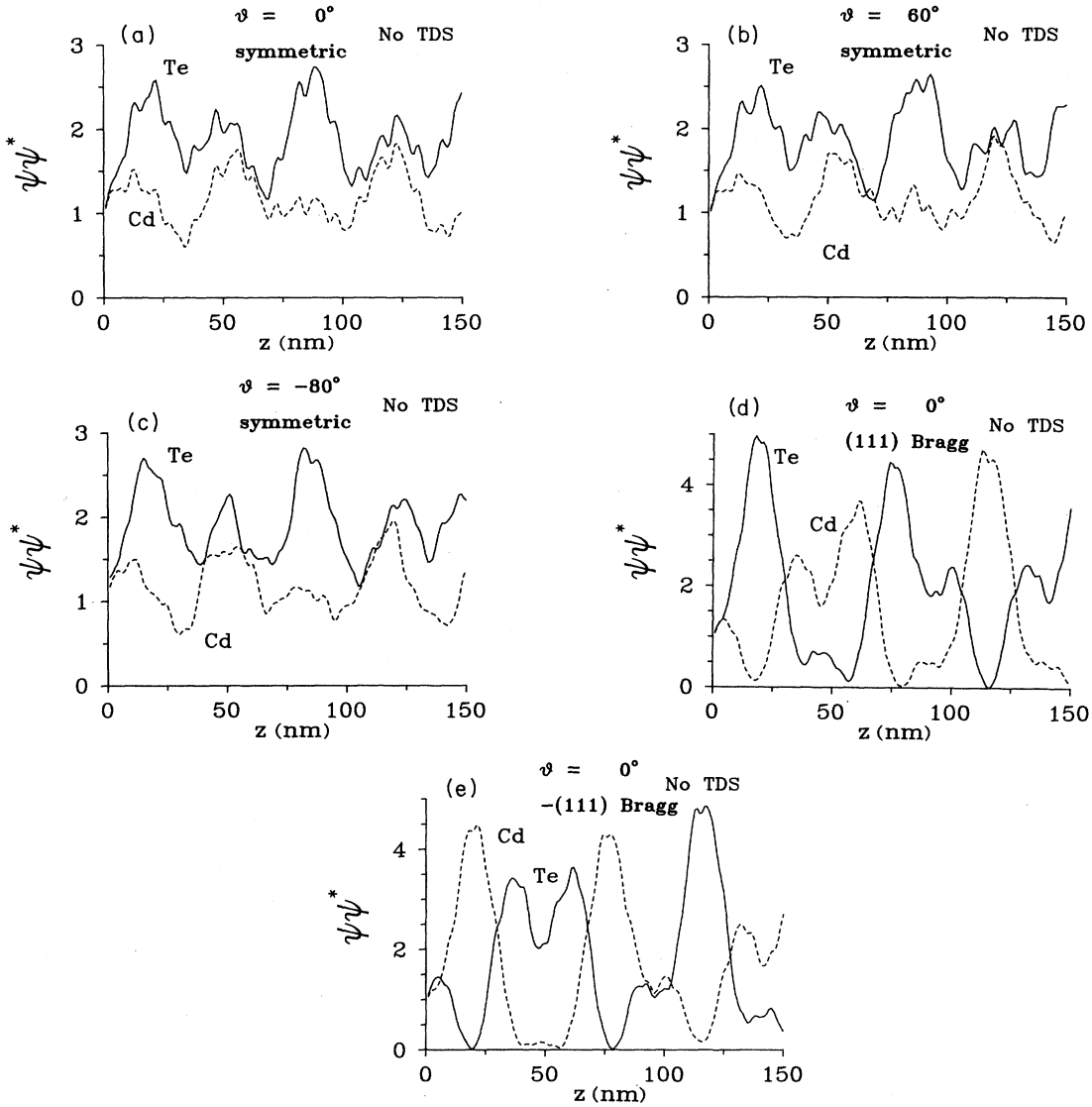


FIG. 5. $\psi\psi^*$ on Cd and Te as a function of depth at 120 keV, for various orientations and surface tilts. Here effects of TDS are neglected. Symmetric orientation: (a) $\theta=0°$, (b) $\theta=60°$, (c) $\theta=-80°$. Surface tilt $=0°$, (d) (111) Bragg orientation, and (e) $(\bar{1}\,\bar{1}\,\bar{1})$ Bragg orientation.

vides an overriding influence on the characteristic x-ray emission ratio under dynamical diffraction conditions. The effect of higher voltage is primarily to make the sample effectively "thinner," the $z$ scale being compressed in proportion to the change in $\chi$ ($2\pi/\lambda$ is 188 $\text{Å}^{-1}$ at 120 keV, 382 $\text{Å}^{-1}$ at 400 keV).

(iii) *Convergent beam electron diffraction.* Figure 9 shows correlation of experiment with calculated diffraction contrast in convergent beam electron diffraction (CBED) discs. Here a thickness of 75 nm is assumed, with anomalous absorption due to TDS at 300 K. This unequivocally identifies the (111) beam, enabling the determination of polarity of a multiply twinned $Hg_xCd_{1-x}Te$ epilayer on GaAs.[28] The Hg concentration was $0.7\pm0.2$ at. %, and scattering due to Hg was ignored in these calculations. Without anomalous absorption, unequivocal correlation is not possible. We have also obtained correlation for thicker samples at 100 K, using a 200-keV beam.

Absolute measurements of CBED intensity, using an energy-filtered elastic beam, have enabled refinement of absorption and structure factors, yielding information on bonding in GaAs.[29] In our raw data, {222} Kikuchi band contrast (which passes through the center of {111} discs in the symmetrical orientation) disallows quantitative correlation through densitometry.

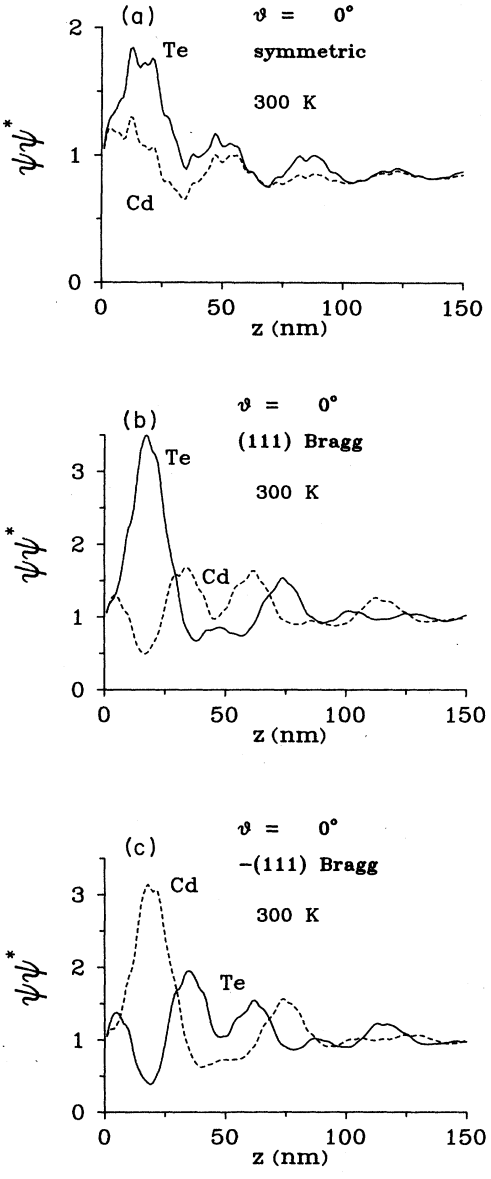


FIG. 6. $\psi\psi^*$ on Cd and Te as a function of depth at 120 keV, for various orientations and no surface tilt. Effects of TDS at 300 K are included. (a) Symmetric orientation, (b) (111) Bragg orientation, and (c) $(\bar{1}\,\bar{1}\,\bar{1})$ Bragg orientation.

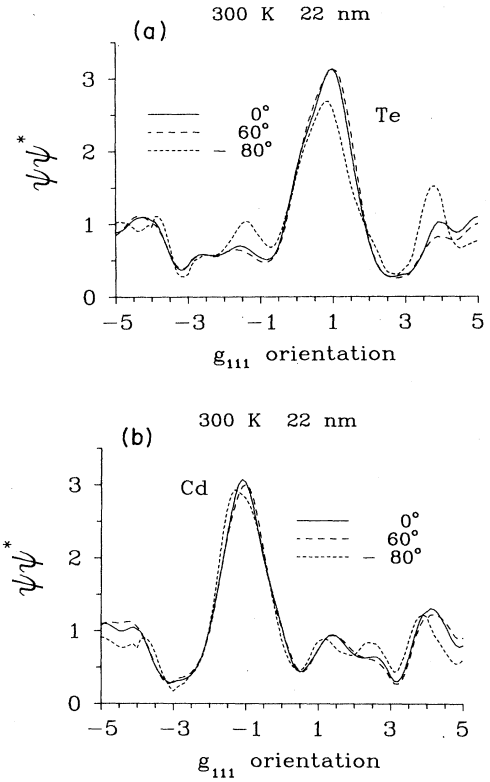


FIG. 7. $\psi\psi^*$ for $z=22$ nm, 300 K, as a function of orientation for (a) Te and (b) Cd for 120 keV electrons.

## VII. CONCLUSIONS

Surface tilts $\theta$ of 60° to −80° have been taken into account in forming the dynamical fast-electron wave function. This affects the mean free path for TDS and $\psi\psi^*$ within the unit cell. However, integrated effects of tilt are small, and it is far more important to take into account dechanneling and anomalous absorption effects due to TDS. Dynamical enhancement of x-ray yields in ALCHEMI-type experiments should vary with surface tilt $\theta$ as shown in Figs. 5 and 7, although $z$-averaged results when coupled with dechanneling due to TDS indicate that these differences are small in ALCHEMI and CBED

experiments. We have also predicted a slight asymmetry in the zeroth-order beam when in the symmetrical Laue orientation, due to surface tilt.

A phenomenon which may be regarded as real-space *pendellosung* occurs for $\psi\psi^*$ on different atoms in noncentrosymmetric structures. For CdTe in the (111) Bragg orientation, $\psi\psi^*$ increases initially with $z$ on Te, but subsequently builds up on Cd with an accompanying decrease on Te (see Fig. 5). This *pendellosung* from one set of atomic sites to the other is linked to reciprocal-space *pendellosung* in diffracted beam intensities, where in addition to amplitudes of both (111) and $(\bar{1}\,\bar{1}\,\bar{1})$ beams oscillating in antiphase with the forward scattered beam, relative maxima of these beams swap between different extinction periods. The nature of real-space *pendellosung* on atom sites inverts for the $(\bar{1}\,\bar{1}\,\bar{1})$ Bragg orientation.

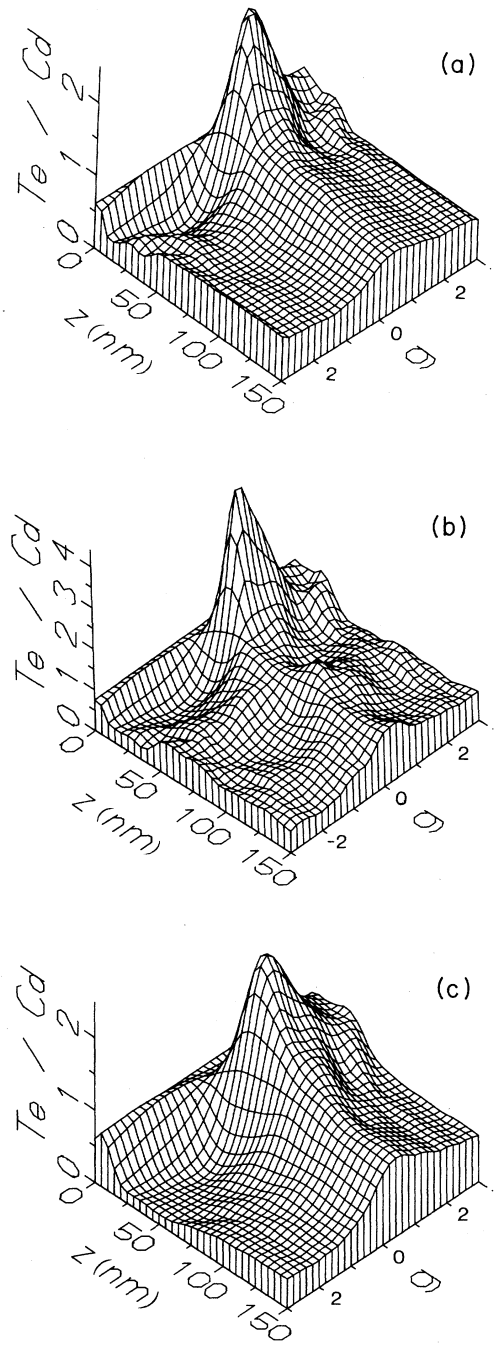


FIG. 8. Three-dimensional plots of the $z$-integrated ratio $\psi\psi^*_{av}$(Te/Cd) for (a) 120 keV electrons, 300 K, (b) 120 keV electrons and no TDS, and (c) 400 keV electrons, 300 K. The orientation $g$ is given in terms of the (111) Bragg orientation.

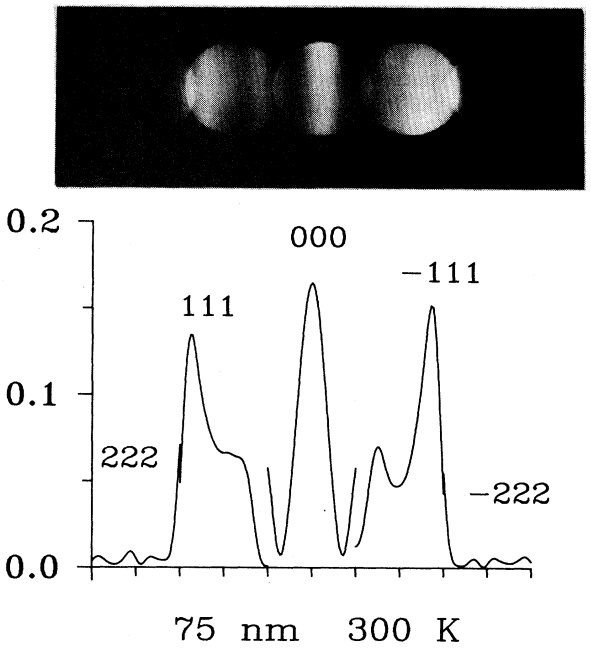


FIG. 9. Correlation of computed CBED contrast with experiment for 120 keV electrons, enabling the determination of crystal polarity.

If no TDS is accounted for, then whether $\psi\psi^*_{av}$ is greater on Te or Cd depends on $z$ for both (111) and $(\bar{1}\,\bar{1}\,\bar{1})$ Bragg orientations. However, if thermal attenuation is included, the ratio $\psi\psi^*_{av}$ (Te/Cd) for the (111) Bragg orientation is greater than unity for all $z$. For the $(\bar{1}\,\bar{1}\,\bar{1})$ Bragg orientation, this ratio is less than unity for all $z$. In other words, the influence of $\psi\psi^*$ within the first extinction period in the crystal will provide an overriding influence on the ratio Te/Cd of characteristic x-ray emission. Thus the interpretation of dynamically induced x-ray fluorescence experiments to determine polarity should be unambiguous, as reported by Taftø,[5] although our computations indicate that this ratio does not change sharply with orientation.

The inclusion of anomalous absorption, using a quantitative Einstein model for TDS, enables correlation between experimental and computed CBED patterns. This also enables direct determination of polarity. ALCHEMI and CBED methods have been successfully applied for the determination of polarity of a {111} film of $Hg_xCd_{1-x}Te$ on {100} GaAs, using beam diameters

20–50 nm. Both methods confirm the growth direction to be $[\bar{1}\,\bar{1}\,\bar{1}]$, or *B* face.[28]

## ACKNOWLEDGMENTS

We are indebted to Denis Lynch and Vic Maslen of CSIRO Division of Materials Science and Technology, Andrew Smith of the Department of Physics, Monash University, Ian McCarthy of the Electronic Structure of Materials Centre, Flinders University, and Tadeusz Warminski of Telecom Research Laboratories for stimulating discussions and advice.

[1]E. A. Hewat, L. DiCioccio, A. Million, M. Dupuy, and J. P. Galliard, J. Appl. Phys. **63**, 4929 (1988).
[2]J. Taftø and J. C. H. Spence, J. Appl. Crystallogr. **15**, 60 (1982).
[3]G. Lu and D. J. H. Cockayne, Philos. Mag. A **53**, 307 (1986).
[4]J. C. H. Spence and J. Taftø, J. Microsc. (Oxford) **130**, 147 (1983).
[5]J. Taftø, Phys. Rev. Lett. **51**, 654 (1983).
[6]C. J. Rossouw and V. W. Maslen, Ultramicroscopy **21**, 277 (1987).
[7]D. Cherns, A. Howie, and M. H. Jacobs, Z. Naturforsch. **28a**, 565 (1973).
[8]J. P. Spencer and C. J. Humphreys, in *Electron Microscopy and Analysis*, Vol. 10 of *Institute of Physics Conference Series* (IOP, Brussels, 1971).
[9]A. J. F. Metherell, in *Electron Microscopy in Materials Science*, edited by U. Valdre and E. Ruedl (Commission of the European Communities, Brussels/Luxembourg, 1975), Pt. II, pp. 397–552.
[10]G. Kastner, Acta Crystallogr. Sect. A **43**, 683 (1987).
[11]L. J. Allen, I. E. McCarthy, V. W. Maslen, and C. J. Rossouw (unpublished).
[12]C. J. Rossouw, S. R. Glanvill, M. S. Kwietniak, G. Pain, T. Warminski, and I. J. Wilson, J. Cryst. Growth **93**, 937 (1988).
[13]G. I. Christiansz, S. Georgiou, S. R. Glanvill, C. Kelly, M. H. Kibel, M. S. Kwietniak, G. N. Pain, C. J. Rossouw, A. W. Stevenson, T. Warminski, B. Usher, L. Wielunski, and S. W. Wilkins, in *Proceedings of the Australian X-ray Analytical Association 7th National Schools and Conference, Perth, 1988*, edited by B. O'Connor (Wiley, Chichester, 1989).
[14]H. A. Bethe, Ann. Phys. (Leipzig) **87**, 55 (1928).
[15]H. S. Kim and S. S. Sheinin, Phys. Status Solidi B **109**, 807 (1982).
[16]H. S. Kim and S. S. Sheinin, Phys. Status Solidi A **108**, 349 (1987).
[17]C. J. Humphreys, Rep. Prog. Phys. **42**, 1825 (1979).
[18]S. S. Sheinin and B. K. Jap, Phys. Status Solidi B **91**, 407 (1979).
[19]C. R. Hall and P. B. Hirsch, Proc. R. Soc. (London) Ser. A **286**, 158 (1965).
[20]C. J. Humphreys and P. B. Hirsch, Philos. Mag. **18**, 115 (1968).
[21]P. A. Doyle, Acta Crystallogr. Sect. A **26**, 133 (1970).
[22]R. W. James, *The Optical Principles of the Diffraction of X-Rays* (Bell, London, 1962), pp. 193–267.
[23]C. J. Rossouw and L. A. Bursill, Proc. R. Soc. (London) Ser. A **408**, 149 (1986).
[24]C. Hsu, S. Sivananthan, X. Chu, and J. P. Faurie, Appl. Phys. Lett. **48**, 908 (1986).
[25]J. S. Reid, Acta Crystallogr. Sect. A **39**, 1 (1983).
[26]P. A. Doyle and P. S. Turner, Acta Crystallogr. A **24**, 390 (1968).
[27]D. T. Cromer and J. T. Waber, Acta Crystallogr. **18**, 104 (1965).
[28]S. R. Glanvill, M. S. Kwietniak, G. Pain, C. J. Rossouw, T. Warminski, and L. S. Wielunski, J. Appl. Phys. (to be published).
[29]J. M. Zuo, J. C. H. Spence, and M. O'Keefe, Phys. Rev. Lett. **61**, 353 (1988).

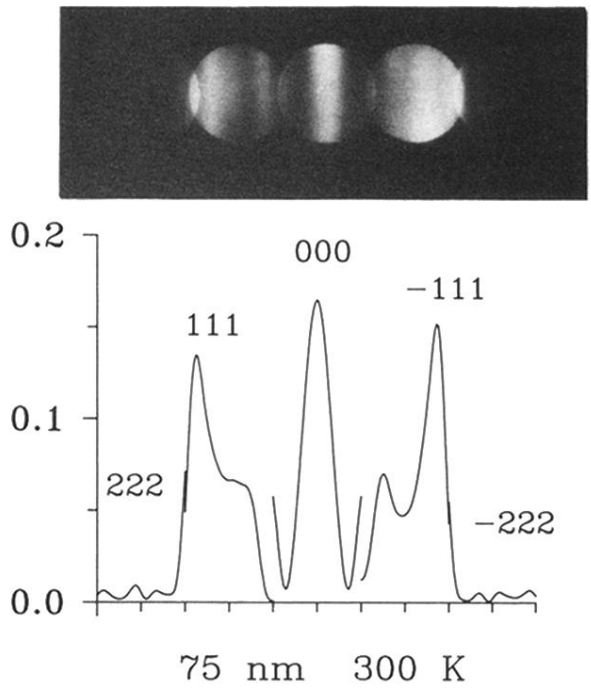


FIG. 9. Correlation of computed CBED contrast with experiment for 120 keV electrons, enabling the determination of crystal polarity.